Three-dimensional elastic full waveform inversion using seismic data from the Sleipner area

Espen Birger Raknes, Børge Arntsen and Wiktor Weibull

Department of Petroleum Engineering and Applied Geophysics, Norwegian University of Science and Technology, Trondheim, Norway.
E-mail: espen.raknes@ntnu.no

SUMMARY

In this study, we demonstrate the application of 3-D isotropic elastic full waveform inversion (FWI) to a field data set from the Sleipner area in the North sea. The field data set consists of a narrow azimuth marine towed streamer survey. The limited maximum offset of less than 2000 m poses strong challenges for the FWI technique, due to the lack of wide-angle wave phenomena, particularly for the deeper sediments. In addition, the lack of information about shear waves implies that only the P-wave velocities can be estimated with some confidence. In this work, the P-wave velocities are inverted using FWI, whereas the S-wave velocities and densities are coupled to the P-wave velocities using empirical relationships. To check the validity of this work flow, a synthetic sensitivity analysis inspired by a well log from the area is performed. In this analysis the difference between acoustic and elastic FWI is also compared. The conclusion from the sensitivity analysis is that, as long as the empirical relationships are not too far away from the true relationships, the elastic FWI is able to resolve the subsurface parameters within an acceptable error margin. Furthermore, the acoustic approximation fails due to the large differences between the elastic and acoustic reflection and transmission coefficients, meaning that elastic FWI is necessary for resolving the parameters satisfactorily. Acoustic and elastic FWI are performed for the field data. The results of the field data example show that elastic FWI produces an elastic model which accurately simulates the observed data, whereas the acoustic FWI produces an acoustic model that includes artefacts, particularly in the upper part close to the sea bottom. Elastic FWI is therefore favourable for short offset seismic streamer data. The estimated elastic P-wave velocity models were used to depth migrate the data. The depth migrated images show improved resolution and continuity compared to those migrated using a model derived from conventional seismic processing methods. At the same time, the P-wave velocities show strong correlations with the corresponding migrated seismic image, which increases the confidence on the inverted model.

Key words: Inverse theory; Controlled source seismology; Computational seismology; Wave propagation.

1 INTRODUCTION

The full waveform inversion (FWI) method is a technique for estimating subsurface elastic parameters using inverse theory. FWI is formulated as an optimization problem that seeks to minimize the dissimilarities between field data and synthetic data. The problem is solved by starting from an initial model which is then iteratively improved using linear approximations to the non-linear problem (Tarantola 1984; Mora 1987; Pratt 1999; Fichtner *et al.* 2006; Virieux & Operto 2009). At the core of the method is the assumption that field data can be approximated by a numerical solution of a wave equation. The interaction between heterogeneous elastic media and the waves is complex and includes mode-conversions,

pre- and post-critical reflections, transmissions, refractions, multiple reflections and surface waves. The choice of the proper wave equation and physical model is thus important in order to accurately honour the complexity of the observed data.

In exploration geophysics, a classical assumption has been to consider the subsurface as a fluid that is parametrized by the density (ρ) and *P*-wave (v_p) velocity. There are two main reasons for this choice. One is that conventional processing focuses on the kinematics of *P* waves, which are well modelled by the acoustic wave equation. The other reason is due to limitations in available computer resources. From a physical point of view, a better assumption is to consider the subsurface as an elastic medium, parametrized by the *S*-wave (v_s) velocity, in addition to ρ and v_p. The elastic

assumption includes, for example, important phenomena like shear waves, that are not predicted by the acoustic assumption, but that are often visible in seismic field data. However, the elastic wave equation is more computationally expensive to solve than the acoustic wave equation, which significantly increases the cost of FWI. Furthermore, including elastic parameters causes an increase in the solution space, which increases the ill-posedness and non-linearity of the inverse problem. The ill-posedness and non-linearity can be mitigated by including more information, such as multicomponent data acquired on the sea floor.

In FWI, the elastic wave equation needs to be solved several times during each iteration. The associated computational cost is one of the main barriers for the applicability of FWI to large-scale 3-D problems (Virieux & Operto 2009). For this reason, field applications of elastic FWI are mostly restricted to 2-D problems. One important difference between 2-D and 3-D wave propagation is in the geometrical spreading factor. By considering the Green's functions of the wave equation, it can be shown that for a point source in a homogeneous medium the amplitudes scale, at a distance r from the source, as $1/r$ in 3-D and $1/\sqrt{r}$ in 2-D (Aki & Richards 2002). Hence, the amplitudes in the synthetic data in the 2-D domain are incorrect compared to the amplitudes in field data. To approximately compensate for the difference in amplitudes, the field data must be scaled prior to the 2-D inversion (Pratt 1999; Ravaut *et al.* 2004). However, the approximate nature of this conversion may introduce artefacts into the inverted parameter models (Auer *et al.* 2013). Hence, one of the benefits of performing FWI in 3-D is that the geometrical spreading factor is correctly modelled. Another benefit of 3-D processing is the proper handling of the out of inline plane events, and the improved resolution along the crossline plane.

The first applications of 3-D FWI in the literature used the acoustic approximation to model synthetic data sets. Sirgue *et al.* (2008) and Ben-Hadj-Ali *et al.* (2008) used frequency-domain implementations to demonstrate FWI in 3-D using synthetic data sets, whereas Vigh & Starr (2008) used a prestack plane-wave time-domain implementation and a synthetic and real data set in 3-D. Ocean-bottom cables (OBCs) have also been used to produce reliable results (Plessix 2009; Sirgue *et al.* 2009). Abubakar *et al.* (2011) used the contrast-source method in 3-D to invert synthetic data sets. Recent developments include more complicated wave phenomena in the computation of the synthetic data set. In global seismology, elastic anisotropic implementations of FWI have been applied on much larger scales than in exploration geophysics to quantify the structure of the upper mantle of the Earth (Fichtner *et al.* 2010, 2013; Tape *et al.* 2010). Warner *et al.* (2013) applied a 3-D anisotropic pseudo-acoustic implementation of FWI on a multicomponent ocean-bottom data set acquired over the Tommeliten field in the North Sea. 3-D isotropic elastic FWI implementations have been used on a small-scale cross-well acquisition (Butzer *et al.* 2013) and a synthetic OBC data set (Vigh *et al.* 2014).

Common for almost all current applications of FWI is that a velocity model is estimated mostly for the shallow area above the reservoir zone of interest. This approach uses long-offset data containing diving waves and wide-angle refracted events with limited penetration depth. Several authors have demonstrated that in this case it is possible to retrieve a v_p model using the acoustic approximation (Pratt 1999; Virieux & Operto 2009). To obtain velocities also at reservoir depth, the reflected part of the wave field must be employed. Barnes & Charara (2009) performed a synthetic study and demonstrated that acoustic FWI is applicable for marine seismic data when short-offset data is used. The requirement for the success of acoustic FWI in this case is that the initial model for v_p

must be accurately estimated. On the other hand, Raknes & Arntsen (2014a) demonstrated using synthetic and real examples that for seismic data that contains primarily reflections, it is crucial to use elastic FWI to obtain reliable inversion results.

In this paper, we demonstrate the application of 3-D isotropic elastic time-domain FWI to a short-offset (<2000 m) seismic field data set consisting primarily of reflected waves. The field data set was acquired over the Sleipner field in the North sea. Prior to the inversion of the field data set, several assumptions must be made. The effect of these assumptions on the results of FWI are investigated in a synthetic sensitivity analysis. Acoustic and elastic FWI are performed for the synthetic and field data to compare the two ways of performing FWI. Results show that elastic FWI estimates an elastic velocity model which reproduces the field data. We show that the *P*-wave velocities can be used to produce conventional depth migrated images with improved resolution and continuity, and common image point angle gathers with improved flatness. A comparison between the *P*-wave velocity model and the available well data shows an improved fit after FWI.

The paper is organized as follows: In Section 2 we briefly describe the theory that underlies FWI, in addition to a short description of the implementation of the method. In Section 3 we describe the area where the field data set was acquired, in addition to details about the data set. Section 4 is devoted to the inversion work flow. The synthetic sensitivity analysis is given in Section 5. The results for the field data set is given in Section 6. The discussions and conclusions are given in Sections 7 and 8, respectively.

2 THEORY

2.1 Full waveform inversion

FWI is a method that tries to find a parameter model that can be used to produce synthetic data that is close to some measured data (Tarantola 1984; Mora 1987; Pratt 1999; Fichtner *et al.* 2006; Virieux & Operto 2009). Let $\mathfrak{M}$ be the space of all admissible models, and $\mathfrak{D}$ the space of all possible data sets. The foundation for the method is the assumption that synthetic data $\mathbf{q}$ in $\mathfrak{D}$ can be generated from an arbitrary model $\mathbf{m}$ in $\mathfrak{M}$ using a wave equation. Let $\mathcal{L} : \mathfrak{M} \to \mathfrak{D}$ be the numerical wave operator which maps $\mathbf{m}$ from $\mathfrak{M}$ into $\mathfrak{D}$. The synthetic data can be generated as

$$\mathcal{L}(\mathbf{m}) = \mathbf{q}. \tag{1}$$

The solution of the problem is given by the inverse operator of $\mathcal{L}$,

$$\mathbf{m} = \mathcal{L}^{-1}(\mathbf{d}), \tag{2}$$

where $\mathcal{L}^{-1}$ is the inverse operator and $\mathbf{d}$ is the measured data. In practice it is not possible to find an explicit expression for the inverse operator.

The standard way of solving the inverse problem in eq. (2) is to consider it as an optimization problem (Nocedal & Wright 2006). We define an objective functional $\Psi : \mathfrak{M} \to \mathfrak{R}^+$ ($\mathfrak{R}^+$ is the space of the positive real numbers), whose purpose is to measure the dissimilarities between $\mathbf{q}$ and $\mathbf{d}$. We require that the solution of the problem, that is, the point where $\mathbf{q}$ and $\mathbf{d}$ are equal, is an extreme point for $\Psi(\mathbf{m})$. Hence, the solution to the problem can simply be expressed as

$$\mathbf{m}' = \arg \min \ \Psi(\mathbf{m}), \tag{3}$$

where $\mathbf{m}'$ is the model in $\mathfrak{M}$ we are searching for. The inverse problem in eq. (3) is non-linear and ill posed.

We use the limited-memory Broyden, Fletcher, Goldfarb, and Shanno (L-BFGS) algorithm (Nocedal & Wright 2006) to search for the extreme points of $\Psi(\mathbf{m})$. The update of the model is given as

$$\mathbf{m}_{k+1} = \mathbf{m}_k - \alpha_k \mathbf{H}_k^{-1} \mathbf{g}_k, \tag{4}$$

where $\alpha_k > 0$ is the step length, $\mathbf{H}_k^{-1}$ is an approximated inverse Hessian matrix, and $\mathbf{g}_k$ is the gradient of $\Psi(\mathbf{m})$ with respect to $\mathbf{m}$ at step k. The L-BFGS algorithm tries to estimate the inverse Hessian matrix using a predefined number of gradients (six in our implementation) from previous iterations, and has proven to be favourable compared to standard conjugate-gradient methods (Brossier *et al.* 2009).

We use a normalized version of the standard least-squares norm as the objective functional (Raknes & Arntsen 2014a). This functional is defined as

$$\Psi(\mathbf{m}) = \frac{1}{2} \sum_{j=0}^{n_s} \sum_{i=0}^{n_r} \|\hat{\mathbf{q}}_{i,j}(\mathbf{m}) - \hat{\mathbf{d}}_{i,j}\|_2^2, \tag{5}$$

where $\hat{\mathbf{q}}_{i,j}(\mathbf{m}) = \mathbf{q}_{i,j}(\mathbf{m})/\|\mathbf{q}_{i,j}(\mathbf{m})\|_2$ is the normalized modelled data, $\hat{\mathbf{d}}_{i,j} = \mathbf{d}_{i,j}/\|\mathbf{d}_{i,j}\|_2$ is the normalized measured data, n_r is the number of receivers in the data set, and n_s is the number of shots in the data set. Here, $\|\cdot\|_2$ is the least-squares norm on $\mathfrak{D}$. The benefit of using this functional is that the real and the synthetic data are automatically scaled within the functional. If a standard least-squares functional is used, then an important preprocessing step is to scale the synthetic and the real data set such that the amplitudes match.

Taking the derivatives of $\Psi(\mathbf{m})$ with respect to $\mathbf{m}$ gives the gradient $\mathbf{g}$,

$$\mathbf{g} = \sum_{j=0}^{n_s} \sum_{i=0}^{n_r} \frac{\partial \mathbf{q}_{i,j}(\mathbf{m})}{\partial \mathbf{m}} \hat{\mathbf{r}}_{i,j}, \tag{6}$$

where

$$\hat{\mathbf{r}}_{i,j} = \frac{1}{\|\mathbf{q}_{i,j}\|_2} \left(\hat{\mathbf{q}}_{i,j} \langle \hat{\mathbf{q}}_{i,j}, \hat{\mathbf{d}}_{i,j} \rangle - \hat{\mathbf{d}}_{i,j} \right) \tag{7}$$

is the residuals vector. Here, $\langle \cdot, \cdot \rangle$ is the inner product on $\mathfrak{D}$. It is worth mentioning that the gradient in eq. (6) is the same as if a global correlation functional is used (Choi & Alkhalifah 2012).

The crucial step in FWI is the computation of $\mathbf{g}$. Using the adjoint state method (Tarantola 1984; Mora 1987; Pratt 1999; Fichtner *et al.* 2006), where the residuals $\hat{\mathbf{r}}_{i,j}$ are reversed in time and back propagated from the receiver positions, the gradients can be calculated using the numerical operator given in eq. (1).

2.2 Implementation

2.2.1 Modelling

We assume that the subsurface of the Earth is an isotropic elastic medium parametrized by the density ρ, the *P*-wave velocity v_p and the *S*-wave velocity v_s. In the following, the Einstein summation convention is used. Wave propagation in the medium is modelled using the equation of motion

$$\rho(\mathbf{x}) \partial_t^2 u_i(\mathbf{x}, t) - \partial_j \sigma_{ij}(\mathbf{x}, t) = f_i(\mathbf{x}, t), \tag{8}$$

and the constitutive relation

$$\sigma_{ij}(\mathbf{x}, t) = \left(\lambda(\mathbf{x}) \delta_{ij} \delta_{kl} + \mu(\mathbf{x})(\delta_{ik}\delta_{jl} + \delta_{il}\delta_{jk}) \right) \partial_l u_k(\mathbf{x}, t), \tag{9}$$

where $\rho(\mathbf{x})$ is the density, $\lambda(\mathbf{x})$ and $\mu(\mathbf{x})$ are the Lamé parameters, $u_i(\mathbf{x}, t)$ is a component in the particle displacement vector, $\sigma_{ij}(\mathbf{x}, t)$ is a component in the stress tensor, and $f_i(\mathbf{x}, t)$ is a component in the force vector (Aki & Richards 2002). Numerically, the equations are solved using an explicit staggered-grid finite difference method (Virieux 1986), with high-order spatial differential operators (Holberg 1987). To simulate non-reflecting boundaries the perfectly matched layer absorbing boundary conditions are used (Berenger 1994; Zhen *et al.* 2009). The reflecting sea surface at the top of the model is approximated using the method described in Mittet (2002).

2.2.2 Gradient computation

To compute the gradient using the adjoint state method, the forward propagating wave field from the source is cross correlated (in time) with a backward propagating field, where the residuals in eq. (7) act as sources at the receiver positions (Tarantola 1984; Mora 1987; Pratt 1999; Fichtner *et al.* 2006). The gradient with respect to v_p for a single shot is given as (Mora 1987)

$$g_{v_p} = -2\rho v_p \int_T \left(\nabla \cdot \mathbf{u}^f \right) \left(\nabla \cdot \mathbf{u}^b \right) \, \mathrm{d}t, \tag{10}$$

where $\mathbf{u}^f = \mathbf{u}^f(\mathbf{x}, t)$ is the particle displacement vector for the forward wave field propagating from the source position, and $\mathbf{u}^b = \mathbf{u}^b(\mathbf{x}, t)$ is the particle displacement vector for the backward residual wave field propagating from the receiver positions.

The major problem with the gradient computation in three dimensions is the requirement for the snapshots for both the forward and the backward propagated wave fields at each time step, as can be seen in eq. (10). A normal procedure in two dimensions is to store the snapshots on disk of the forward wave fields during the forward modelling, and read them into memory when they are needed. In three dimensions, this procedure requires extreme amounts of disk space, and is therefore not affordable in practice for the number of grid points and the specifications of the computer cluster used here.

To overcome this problem the following strategy is used. During forward modelling, the forward wave fields in eq. (10) are stored at the six boundaries. In addition, to prevent the loss of wave fronts that have not reached the boundaries at the end of the forward modelling, full snapshots of all wave fields in the computational domain are stored at the last time step. When the backward propagating wave fields are computed, the forward propagated wave fields are reconstructed in reverse-time by using the stored wave fields as boundary conditions. This strategy effectively reduces the storage requirements of the gradient computation at the cost of one additional reverse-time modelling. An alternative method to reduce the storage requirements is the optimal checkpointing method (Griewank & Walther 2000; Symes 2007). This method increases the total computational cost compared to the above mentioned method due to the extra modelling steps required between each checkpoint in time.

3 THE SLEIPNER FIELD DATA SET

3.1 Acquisition

The Sleipner area lies west of Norway in the North Sea. It consists of the Sleipner Vest gas field and the Sleipner Øst condensate field, in addition to some smaller fields (Fig. 1). The gas produced from the Sleipner Vest field contains CO_2, which due to environmental and economical reasons is stripped away from the gas and injected
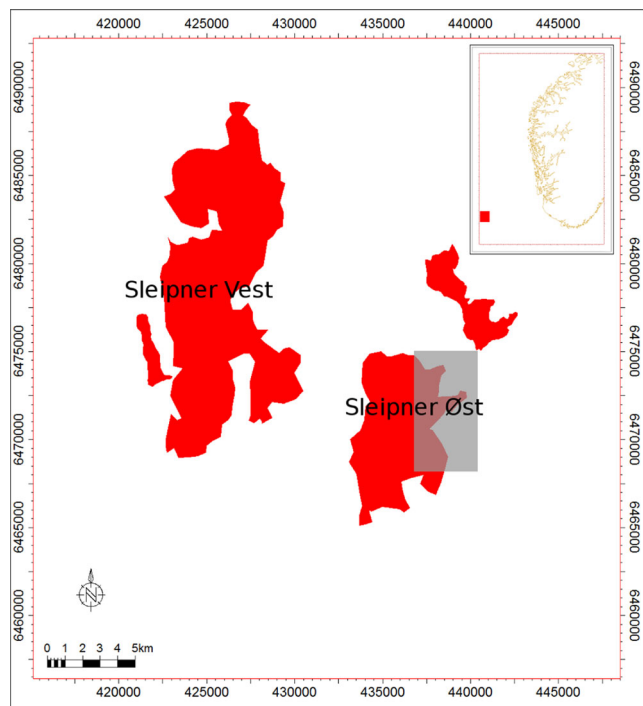
Figure 1. A map of the Sleipner area in the North Sea west of Norway. The Sleipner Vest field is a condensate field, and the Sleipner Øst field is a gas field. CO_2 is stripped from the gas and injected at the Sleipner Øst facility. The grey shaded square is the area where the data set that we use in this study was acquired, and it covers the underground formations where the CO_2 is injected. The coordinate system is UTM zone 31N. (Map courtesy of the Norwegian Petroleum Directorate.)

into the Utsira formation at the Sleipner Øst facility (Furre & Eiken 2014). The Utsira formation consists of a 200–300 m thick high porosity sandstone layer at approximately 700–800 m depth, and the overburden consists of clay-rich sediments (Chadwick *et al.* 2004; Furre & Eiken 2014). In 1994, before the injection of gas started, a 3-D narrow azimuth streamer survey was acquired over the area. This data set was acquired using five receiver cables towed at a depth of 8 m. The cable length was 3000 m and the separation between each cable was 100 m. The source was two 3400 in³ air gun arrays towed at 6 m depth, with shooting interval 18.75 m (flip-flop shooting). The recording length for each shot was 5.5 s.

3.2 Preprocessing

The contractor had applied the following processing steps to the data set before it was released:

(i) Restricted maximum offset to 1700 m,
(ii) Reduced the recording length to 2.3 s,
(iii) Applied a signature deconvolution and swell noise filter,
(iv) Applied a low-cut filter at 6.0 Hz,
(v) Sampled the time-step to 2.0 ms,
(vi) Gained the data using a t^2 scaling factor.

3.3 Shot gathers

Fig. 2(a) shows the first 1.4 s of a shot gather from the centre cable. It can be seen immediately that at near offset, that is, below 400 m offset, the arrivals are mainly reflections and multiples. For offsets over 400 m the data is dominated by refracted arrivals.

These arrivals are a mixture of turning and head waves, surface waves, and post critical reflections, in combination with their ghosts and surface related multiples. Hence, the direct wave is difficult to distinguish from the other arrivals. In the 6–8 Hz filtered version of the shot gather (Fig. 2b) all the distinct arrivals are smeared out. In particular, the refracted and the direct arrivals are smeared together. As the frequency band is increased (Figs 2c and d), the number of resolvable events in the data set increases. At 15 Hz the refracted arrivals are easily seen, as well as the near offset reflections.

3.4 Well log

An exploration well was drilled in the western part of the study area (Fig. 4a). The vertical profile of the *P*-wave velocity sonic log is given in Fig. 3. The well log is partly edited in the intervals where there are no horizontal oscillations. From the figure we observe three high velocity layers at approximately 600, 800 and 1100 m. The Utsira formation lies between the two high velocity layers at approximately 800 and 1100 m depth.

4 INVERSION WORK FLOW

4.1 Inversion area

To restrict the total computational cost of performing the inversion, we choose a subset from the acquisition area of the survey. The size of the study area is approximately 2.0 km × 8.0 km. In total, 1704 shots were acquired inside the area. We decimate the field data set by picking every second shot such that the final data set consists of 852 shots and 570840 data traces. The shots are spread over eight shot lines (Fig. 4a), and the shot interval is approximately 37.5 m. As can be seen in Fig. 4(a), one of the lines was shot in the opposite direction compared to the rest of the lines. In what follows, all coordinates are given with respect to the coordinates in Fig. 4(a).

In Fig. 4(b) a fold plot of the data set is given. This plot is made by counting the number of common-midpoints (CMP) into bins of size 25 m × 25 m. Under the assumption of a plane horizontal layered Earth, the fold plot is a measure of the redundancy with which each position is illuminated by the acquisition geometry. As can be seen in the map, the fold is locally non-uniform. This is due to irregular acquisition, caused mainly by the feathering of the streamers by the ocean currents during the seismic survey. Since the fold is an indication of how many traces are summed together to form the gradient, the irregular distribution of the fold at each surface position might thus contribute to add an acquisition imprint on the gradient of FWI.

4.2 Data regularization

The field data set must be regularized to fit into the inversion scheme. The data regularization consists of the following steps: (i) choosing the frequencies to be used in the inversion, (ii) moving the data traces into the numerical grid, (iii) reverse the preprocessing sequences applied by the contractor, and match the synthetic data with the field data.

Since FWI is solved using a local optimization method, it may converge to a local minimum a certain distance from the global minimum (Fichtner 2011), or the data may be cycle-skipped (Virieux & Operto 2009). To prevent this from happening, we perform sequential inversion runs, where we in each run gradually increase the frequency band for the data set (Bunks *et al.* 1995). By using the
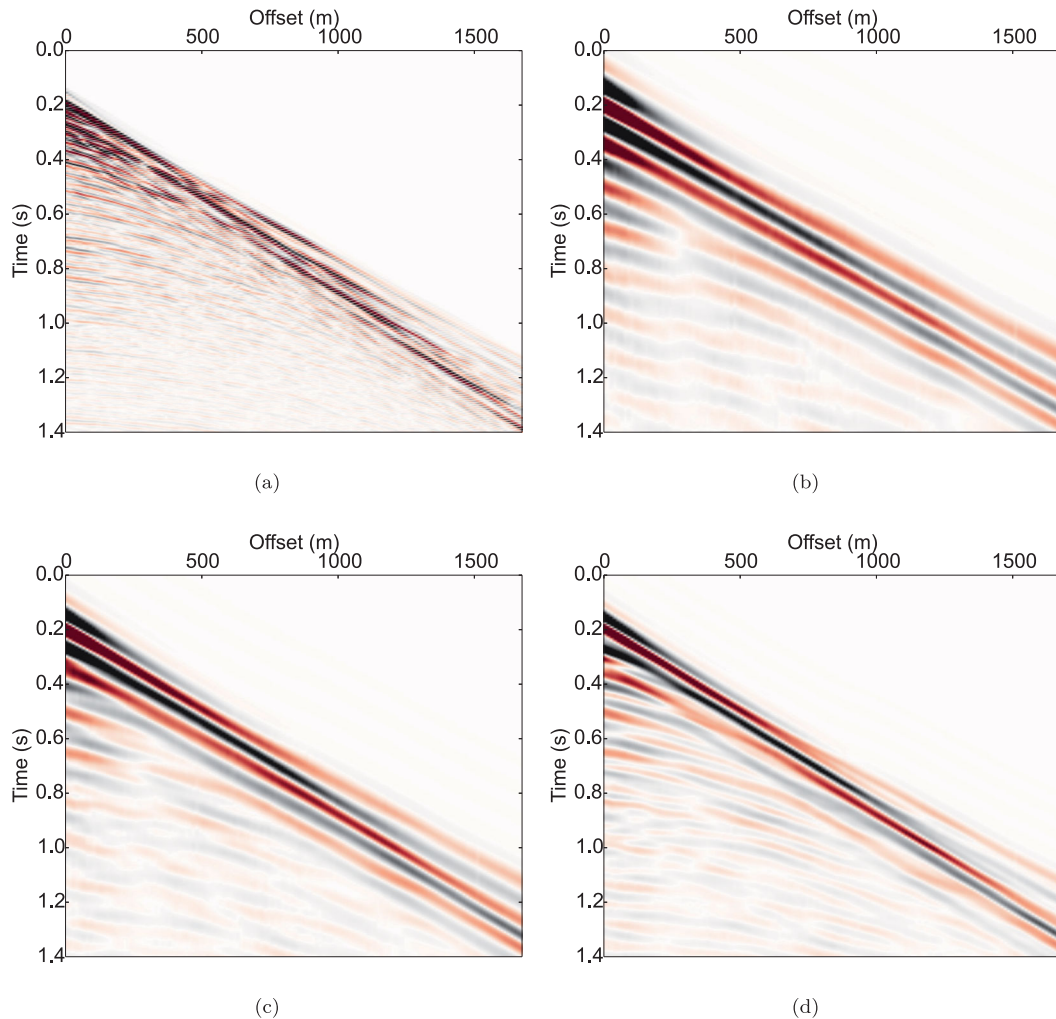
Figure 2. Shot gather from the inversion area for different frequency bands: (a) The full frequency band, (b) 6–8 Hz, (c) 6–11 Hz and (d) 6–15 Hz.
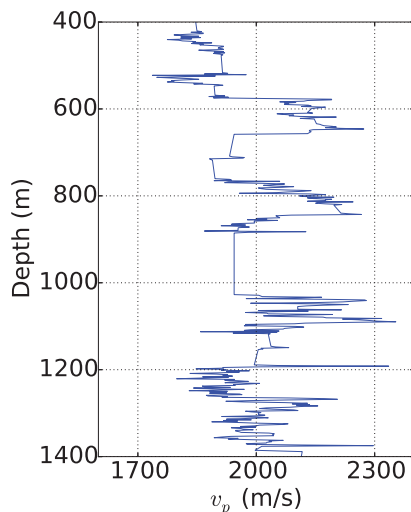

Figure 3. Sonic well log from the inversion area (see Fig. 4a for the position of the well). The log is partly edited.

method described by Sirgue & Pratt (2004), we use the following frequency bands: 6–8 Hz, 6–11 Hz, and 6–15 Hz in the inversion.

Since the data set was acquired on a continuous and irregular grid, each receiver must be moved to the numerical grid used in the inversion. Due to the low frequencies used in the inversion, we use a simple data binning technique where each receiver trace is moved to the nearest grid point without amplitude or phase corrections. For each receiver, the distance to all four corners in the numerical grid cell is computed, and the receiver is moved to the nearest cell corner. The average distance a trace is moved is 4.8 m, whereas the maximum and minimum distances are 8.8 m and 0.0 m, respectively.

Unfortunately, the only preprocessing step that is reversible is the time gain applied to the data set. Each trace in the data set is multiplied by t^{-2}. To check that the decay is correct, the field data set is compared to the synthetic data. Interpolation is used to reduce the time sampling to 1.0 ms, which is the time sampling used in the modelling. The last step is to add time delay to the data, such that the first arrivals in the field data set match the synthetic counterpart.

4.3 Source wavelet estimation

To estimate the source wavelet, we stack the near-offset traces from several shots, and mute away everything but the direct arrival. We use the resulting data set as input to FWI, where we invert for the source wavelet in the time-domain. Since we are using near-offsets, we use small parameter models in the inversion, such that the estimation of the source wavelet is a relatively fast procedure.
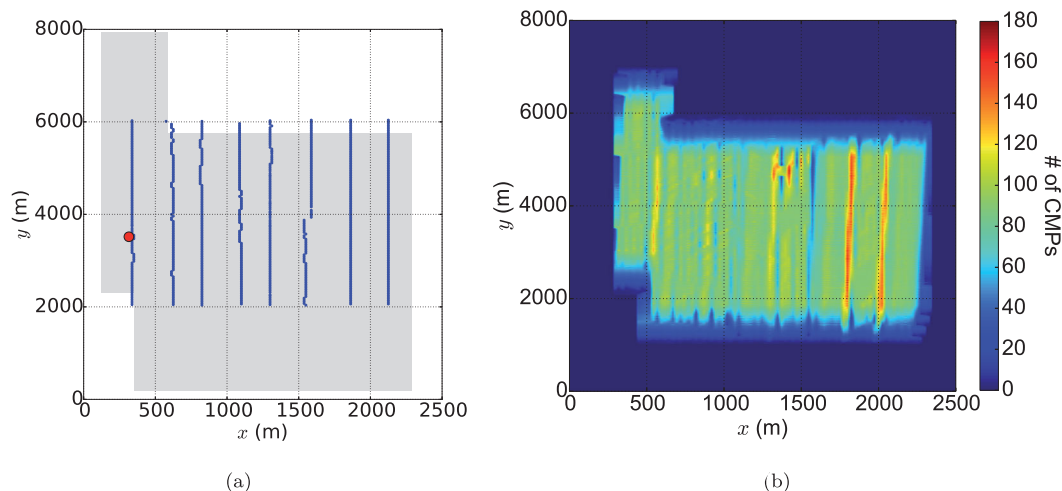
Figure 4. (a) Overview of the area used in the inversion. The blue lines are source positions, and the grey shaded area is the position for all the receivers. The red circle is the position of the exploration well. (b) Fold plot of the seismic data.

Since several frequency bands are used in the inversion, a source wavelet is estimated for each frequency band.

4.4 Inversion strategy

Inverting for three elastic parameters using FWI is difficult, particularly when working with streamer data (Raknes & Arntsen 2014b). Therefore, we use FWI to invert for v_p and update ρ and v_s using empirical relationships. Coupling densities and *S*-wave velocities to the *P*-wave velocities has proven to be a successful approach in situations where information about shear waves are not present in the data (Shipp & Singh 2002; Raknes & Arntsen 2014a).

The choice of empirical relationships is not straightforward since it is difficult to find a perfect match for all rock types (Mavko *et al.* 2009). We use the well-known Gardner's relationship (Gardner *et al.* 1974), which is valid for many rock types, to link ρ to v_p. This relationship is given as

$$\rho = \begin{cases} 1000 & \text{if } v_p \leq 1500, \\ 310v_p^{0.25} & \text{if } v_p > 1500. \end{cases} \tag{11}$$

For the relationship between v_s and v_p we use the so-called 'mud-rock' line (Castagna *et al.* 1985), which is given as

$$v_s = 0.862v_p - 1172. \tag{12}$$

In the above equations $[\rho] = \text{m kg}^{-3}$ and $[v_p] = [v_s] = \text{m s}^{-1}$.

The total computational cost is reduced by using the cyclic shot sub sampling method (Ha & Shin 2013). All shots in the data set are divided into different groups. In each iteration only shots from one group are used. In the next iteration, a new group of shots is used. When all groups have been used, the model is covered by each shot at least one time. Hence, the computational cost is reduced by a factor equal to the number of groups.

To reduce the computational cost even more, we divide the full model into smaller models such that each local model includes only a single shot and the corresponding receivers. This procedure has major impact on the runtime for computing the synthetic data and the gradients for each shot. Even though neighbouring local models are overlapping, artefacts due to low aperture will be visible in the results.

5 SYNTHETIC SENSITIVITY ANALYSIS

To investigate different aspects of the inversion work flow presented in Section 4, we use a synthetic model inspired by the well log from the inversion area (Fig. 3). In the synthetic model, the magnitude of the elastic parameters increases with depth, and three layers with large velocities are included to mimic the layers that are visible in the true well log (Fig. 5). The parameters are linked using eqs (11) and (12). To reduce the error sources in the inversion due to a complicated model, the synthetic model only varies vertically. In the following, we study the sensitivity with respect to the following aspects: the cyclic sub sampling method, the difference between elastic and acoustic FWI, and the influence of wrong empirical relationships used in the inversion.

We simulate a conventional 3-D streamer survey consisting of 316 shots with 100 m shot interval. The shots are spread over four sail lines. The distance between each line is 500 m. Five receiver cables with length 1700 and 12.5 m receiver interval are towed behind the source. The distance between each receiver cable is 100 m. The source wavelet is a Ricker wavelet with 10.0 Hz centre frequency. The model is 1400 m in depth, and 2500 and 6000 m in the horizontal directions. The grid sampling is 12.5 m in all directions, such that the numerical grid for each parameter consists of approximately 10.7 million points. The initial model is created by applying a smoothing operator on the true model.

We start the sensitivity analysis by testing the shot sub sampling method. Two inversion runs are performed. In the first run all 316 shots are used in each iteration, whereas in the second run four groups of shots are used. There are 79 shots with a shot distance of 400 m between each shot in each group. The true empirical relationships (eqs 11 and 12) are used to update ρ and v_s in each iteration. Fig. 5 shows vertical profiles of the true, initial and inverted model for the three elastic parameters with and without sub sampling used in the inversion. We observe that there are side lobes at each interface, which is expected due to the frequency content of the data. The results obtained with the shot sub sampling method have lower magnitudes than the results obtained without sub sampling. It is in the first 800 m in depth the differences are present, below 800 m there are no significant differences between the two inversion runs. The conclusion on this test is that, despite the small difference in magnitude in the model updates, the shot sub sampling method is
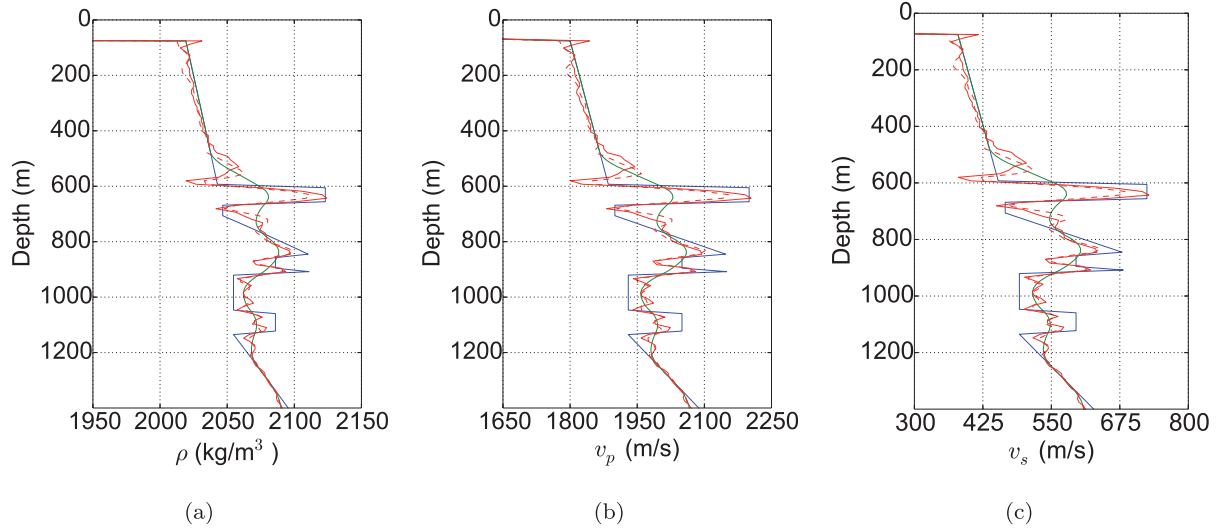
Figure 5. Vertical profiles of the models in the synthetic test for the shot sub sampling method. (a) ρ, (b) v_p and (c) v_s (blue line: true model, green line: initial model, solid red line: inverted model without shot sampling, dotted red line: inverted model with shot sampling).
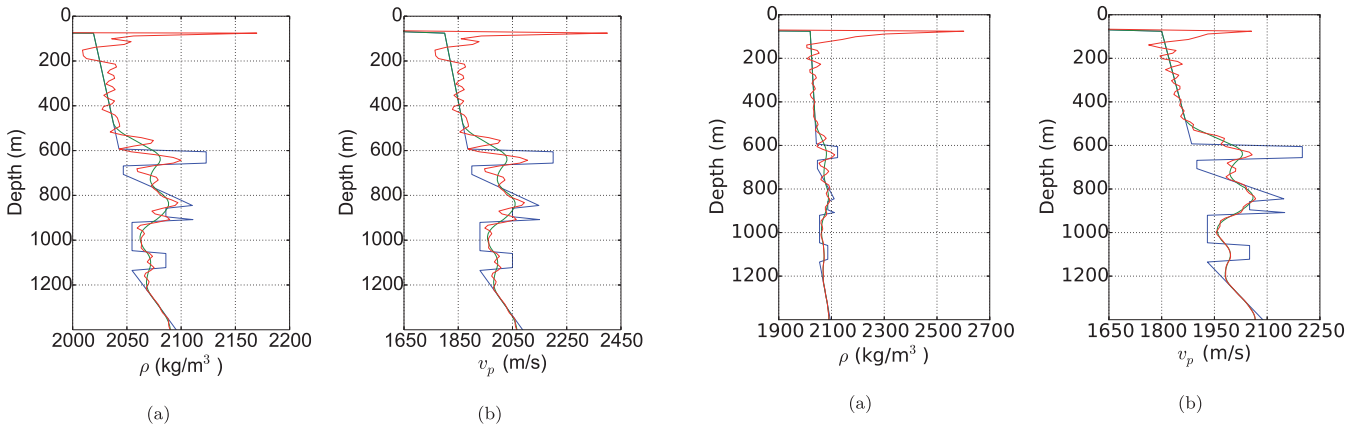

Figure 6. Vertical profiles of the models in the synthetic example for acoustic inversion when v_p is inverted for and ρ is updated using the empirical relationship. (a) ρ, and (b) v_p (blue line: true model, green line: initial model, solid red line: inverted model).

Figure 7. Vertical profiles of the models in the synthetic example for acoustic inversion when v_p and ρ are inverted for. (a) ρ, and (b) v_p (blue line: true model, green line: initial model, solid red line: inverted model).

favourable due to reduction in the overall computational cost, and is therefore used in the remaining tests.

An important question is if there is a difference between acoustic and elastic FWI using near-offset data. We test two different ways of performing acoustic FWI on elastic data. In the first test we invert for v_p and update ρ using the true empirical relationship (eq. 11). In the second test both v_p and ρ are inverted for using FWI. The results for the first test are given in Fig. 6, whereas the results for the second test are given in Fig. 7. From the figures we observe that the acoustic FWI has problems with estimating correct amplitudes for the two parameters in the sea bottom. Moreover, the amplitudes further down in the models are wrong, in addition to being slightly shifted downwards in depth. The problems in the sea bottom can be explained by the differences in the reflection and transmission coefficients between an acoustic and elastic medium.

We now test what happens with the inverted parameter models if wrong empirical relationships are used in the updates. In the first test, we use a v_s relationship that differs from the true relationship. The updates of v_s are done using (Mavko *et al.* 2009)

$$v_s = 0.842v_p - 1099, \tag{13}$$

and the ρ model is updated using the true relationship in eq. (11). From the final inverted models in Fig. 8 we observe that both the ρ and v_p models are influenced by the wrong v_s update. The interfaces somewhat follow the pattern of the true model, but the amplitudes of the updates are wrong. At the deepest part in the model, the inversion is hardly able to perform any updates.

In the next test, we use a wrong relationship for both v_s and ρ. The updates for ρ are given as

$$\rho = \begin{cases} 1000 & \text{if } v_p \le 1500, \\ 250v_p^{0.25} & \text{if } v_p > 1500, \end{cases} \tag{14}$$

and the updates for v_s are done using eq. (13). The final inverted models are given in Fig. 9, from which we observe that the inverted models for v_p and v_s are similar to the models obtained in the test where only the v_s relationship was wrong. From this test, it may look like a wrong update in ρ is less important than a wrong update in v_s.

From the sensitivity analysis it is clear that as the depth is increased, the ability of FWI to update the models is reduced. Thus, the resolution at the deepest parts in the models are small,
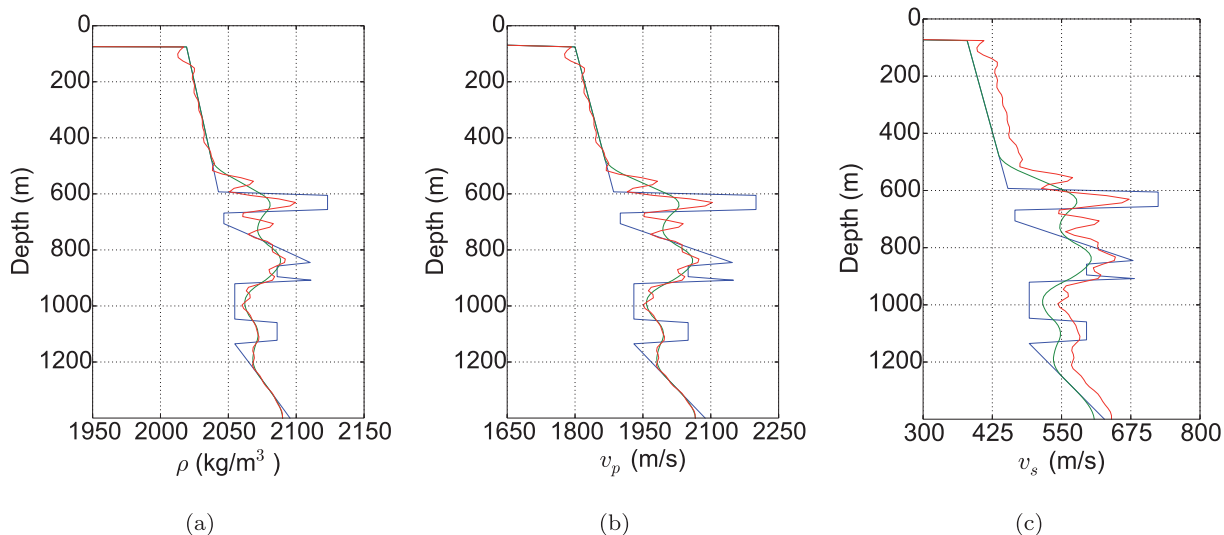
Figure 8. Vertical profiles of the models in the synthetic example when wrong v_s relationship is used in the updates. (a) ρ, (b) v_p and (c) v_s (blue line: true model, green line: initial model, solid red line: inverted model).
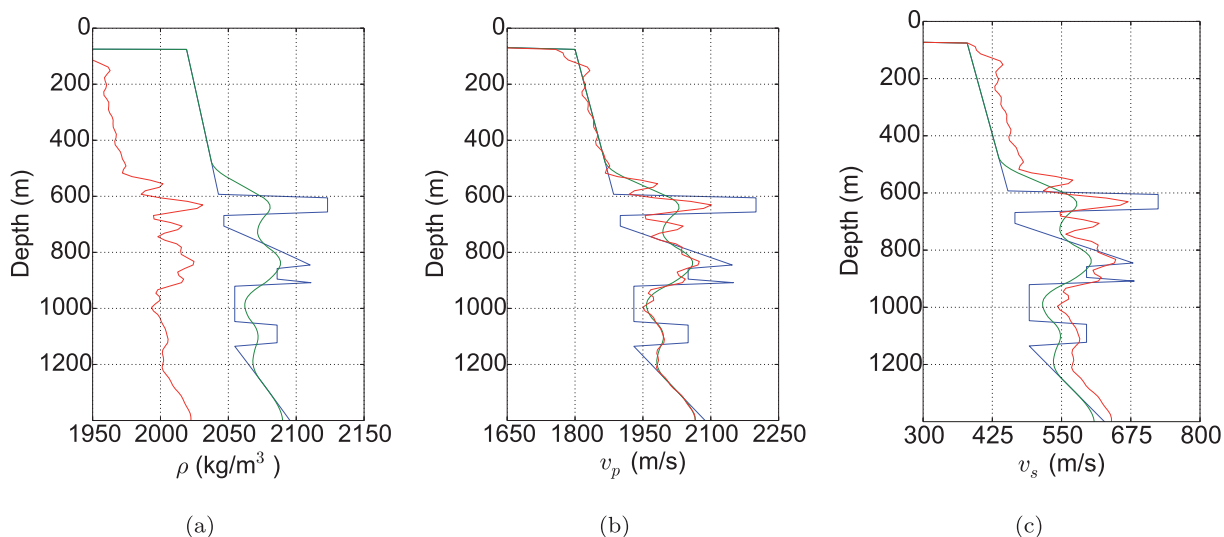

Figure 9. Vertical profiles of the models in the synthetic example when both ρ and v_s are updated using wrong empirical relationships. (a) ρ, (b) v_p and (c) v_s (blue line: true model, green line: initial model, solid red line: inverted model).

compared to the shallower parts. This is due to the short offsets in the data. In the best case, below 1000 m depth the inversion somewhat catches the interfaces, but the amplitudes of the updates are small. In all tests, the first 500 m of the results demonstrate an issue with FWI: even though the initial model is identical to the true model in this region, the models are updated during the inversions. The result for the acoustic inversion demonstrates that elastic inversion is preferable for this type of data. In general, if correct empirical relationships are used to update the parameters not inverted for, then FWI is capable of estimating the parameters within the accepted resolution for the frequencies used in the inversion. On the other hand, wrong relationships yield lower resolution in the final inverted models. Finally, it is worth mentioning the impact of the source and receiver geometry on the inverted models. The updates show an imprint of the sail lines. In the scenario of narrow azimuth acquisitions, FWI shows the highest resolution along the sail lines, and the worst resolution in between the lines.

6 INVERSION OF THE SLEIPNER DATA SET

The starting point for the inversion of the field data set is the estimation of the source wavelet. Obtaining a good approximation of the source wavelet is important for FWI. An inaccurate estimate of the source wavelet will most likely result in artefacts in the inverted model, but can, in the worst case, result in convergence into a local minimum. The estimated source wavelets and their spectra are given in Fig. 10. We observe that the shape of the wavelets does not differ significantly, and that the source spectrum does not have notches. The wavelets are similar to bandpass filtered Ricker wavelets with reversed polarity. Before the wavelets are used in the inversion, they are tested on arbitrary shots in the data set. Some small modifications of the source wavelets are necessary, to yield a better match between the real and synthetic shots.

Prior to the inversion, the 852 shots are divided into four equal-sized groups. The distance between each shot in one group is
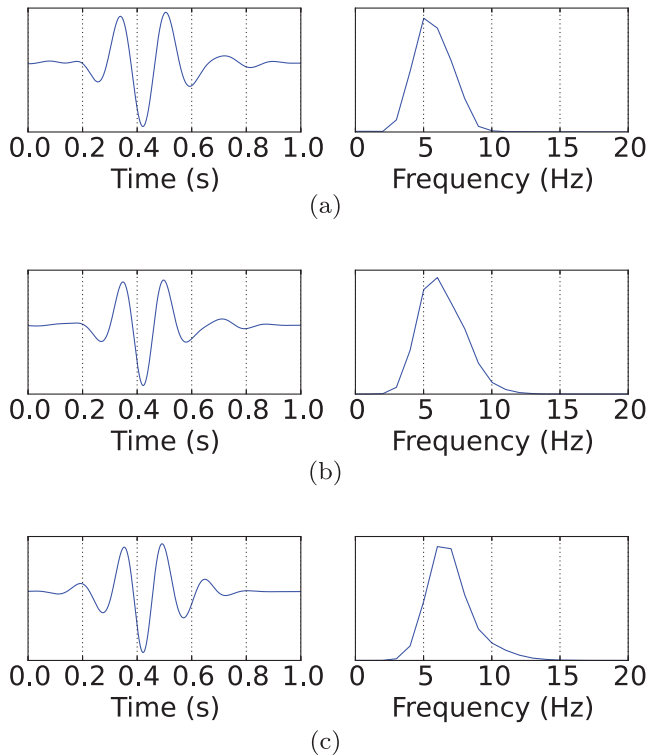
Figure 10. The estimated source wavelets and their spectra in the different frequency bands: (a) 6–8 Hz, (b) 6–11 Hz, and (c) 6–15 Hz.

approximately 150 m. The initial model (Figs 11a and 12a) is 1437.5 m deep, and 2500 m and 8250 m in the horizontal directions, and was made using traveltime tomography. The grid sampling is 12.5 m on all axes such that each elastic parameter model consists of approximately 15 million grid points. Three inversion runs are performed. For the first run, where the 6–8 Hz data is used, the initial model is used. For the two other runs the final model from the previous inversion run is used as initial model. Vertical slices of the initial model and the inverted models for each frequency band are given in Figs 11 and 12. We observe that as the frequency content is increased, the inversion sharpens up the models and introduces several clear structures. The clearest structures are the high velocity layer at approximately 600 m depth, and the flat layers at approximately 900 m and deeper. Some oscillations are visible in the sea bottom. By comparing the models for the 6–15 Hz inversion (Fig. 11d) with the model from the 6–8 Hz inversion (Fig. 11b), we observe that in the former model a more distinct layer is visible at approximately 400 m depth. There are small differences between the two last inverted models.

Trace comparisons of the synthetic data and the field data for the three frequency bands are shown in Fig. 13. In general, the final synthetic data show a better fit to the field data than the initial synthetic data. There is no perfect match between the final data and the field data. The small time shifts visible can be explained by the positioning of the traces into the numerical grid. Furthermore, the amplitude differences in the primary reflections are a result of the processing sequence applied to the field data, and a not perfectly resolved sea bed.

As in the synthetic sensitivity analysis, two acoustic inversions of the 6–8 Hz data set are performed to compare elastic and acoustic
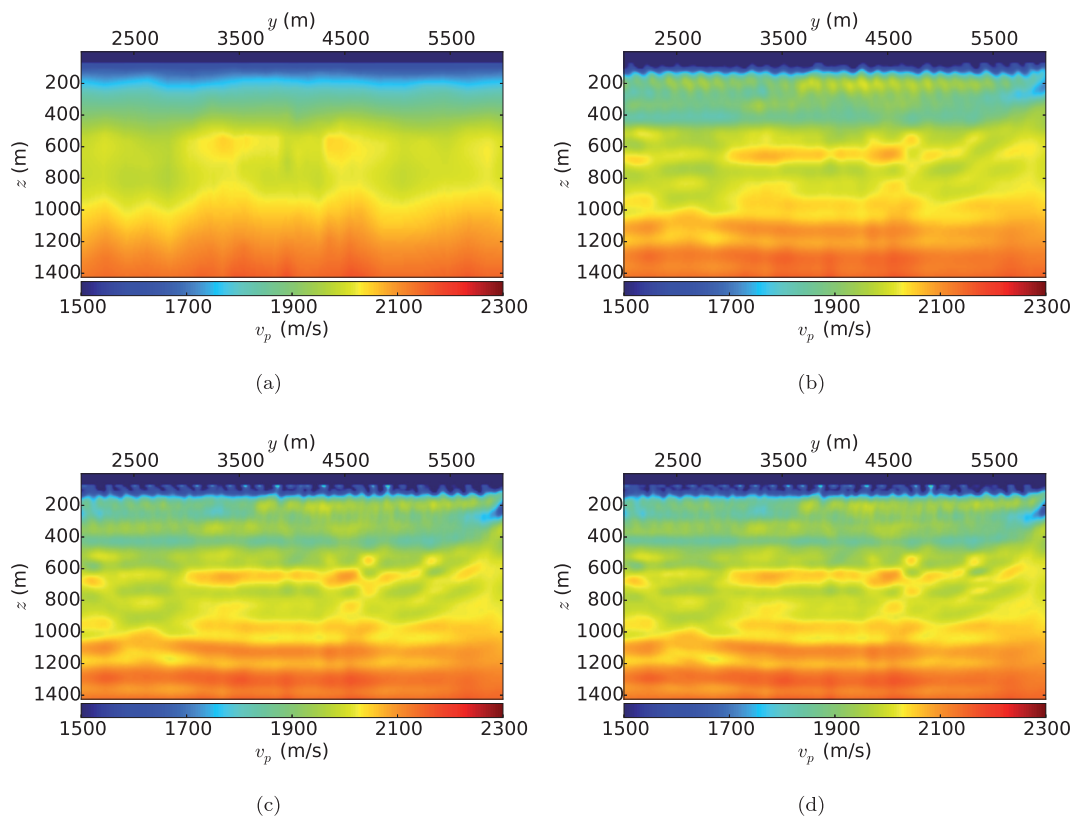
Figure 11. Vertical slices at $x = 1162.5$ m (see Fig. 4a) of the v_p model for the field data set: (a) initial model, (b) inverted model using the frequency band 6–8 Hz, (c) inverted model using frequency band 6–11 Hz, and (d) inverted model using frequency band 6–15 Hz.
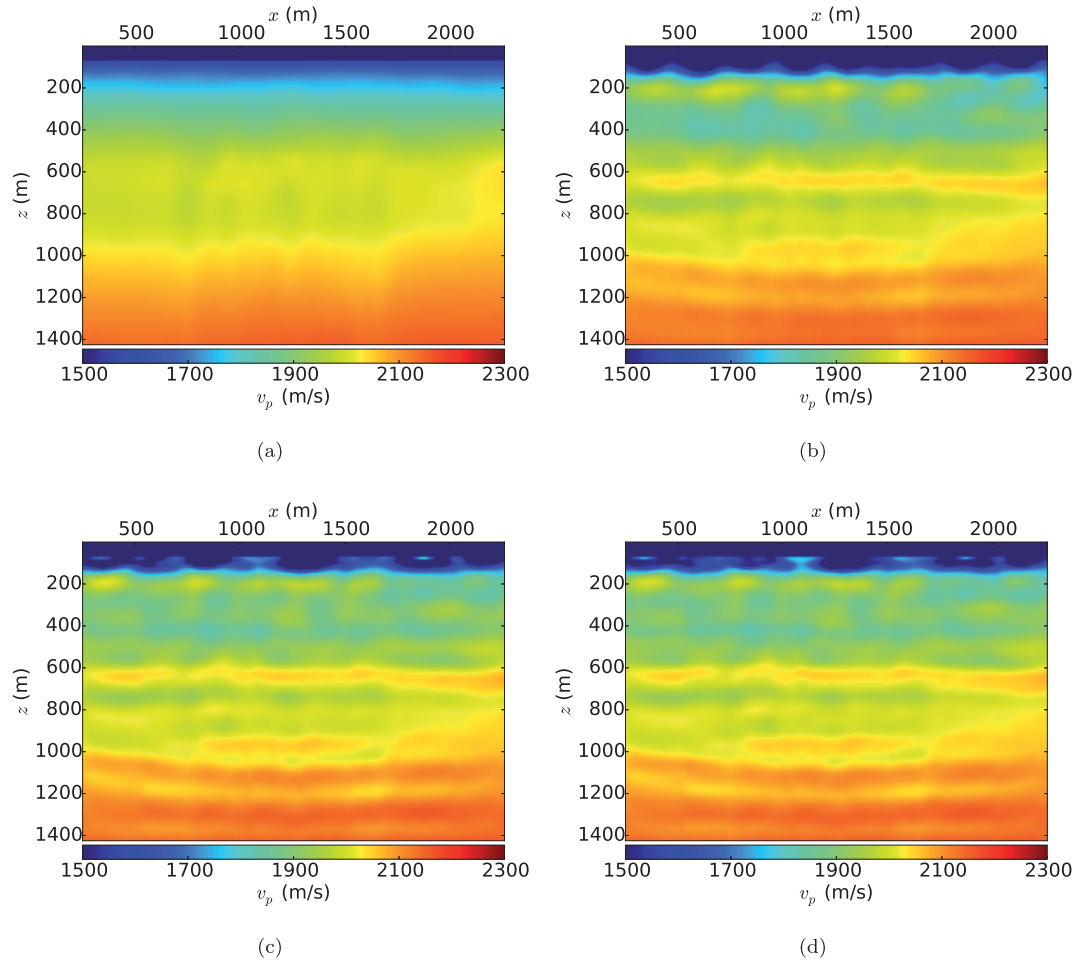
Figure 12. Vertical slices at $y = 4000.0$ m (see Fig. 4a) of the v_p model for the field data set: (a) initial model, (b) inverted model using the frequency band 6–8 Hz, (c) inverted model using frequency band 6–11 Hz, and (d) inverted model using frequency band 6–15 Hz.

FWI. In the first inversion run, FWI is used to invert for v_p whereas ρ is updated using eq. (11). In the second acoustic inversion run, both v_p and ρ are estimated using FWI. The inverted acoustic models are given in Fig. 14. Both inverted acoustic models have artefacts in the regions down to approximately 600 m depth. There are more artefacts in the inverted models for the second inversion. The artefacts are not visible in the inverted elastic model. The overall structure is similar in the two acoustic models. Compared to the inverted elastic model the interfaces in the models are slightly shifted downward in depth. Furthermore, the layers at 400 m and 500 m depths are not well resolved in the acoustic models.

Due to the artefacts in the upper parts of the inverted acoustic models, inversion using the two other frequency bands are not performed since these artefacts will be further emphasized.

To compare the initial model with the final inverted elastic model, we create seismic images using a standard 3-D implementation of the one-way migration method [see for instance Etgen *et al.* (2009) and the references given therein]. Fig. 15 shows a comparison of a shallow horizontal seismic image and the corresponding v_p model for the initial and inverted models. The most obvious improvement between the initial and final models is the focusing of the channel system. The major channel is clearly visible in both the final image and the inverted velocity model. The channel in the lower right corner is also better resolved in the final images. In addition, a

channel-like event is better focused in the upper part of the final image than in the initial image. On the overlay plots, we observe that there is a clear correlation between the velocity model and the seismic image for the final model. This correlation is not visible in the initial model. The acquisition footprints are clearly visible in both the seismic images and the velocity models.

In Fig. 16 a similar comparison for a horizontal slice at a deeper depth is given. By comparing the initial seismic image with the final seismic image, we observe that the channel in the lower left of the slice becomes continuous in the final image. The shape of the channel is also slightly changed between the two images. The overlay plot illustrates that there is a good correlation between the high velocity structure and the final seismic image at the lower right in the plots. Moreover, the events at approximately $y = 2500$ m and $x = 1000$ m in the final seismic image correlate with a low velocity zone in the v_p model.

Vertical slices through the initial and final image cubes are shown in Fig. 17. Specific areas where there are improvements between the images are marked with arrows in the plots. The focusing of the shallow channels is clearly visible. The interface at approximately 400 m depth is better focused and more continuous in the final image compared to the initial image. The same can be said about the other interfaces at deeper depths. In general, the seismic image created using the final inverted model is less noisy and with better
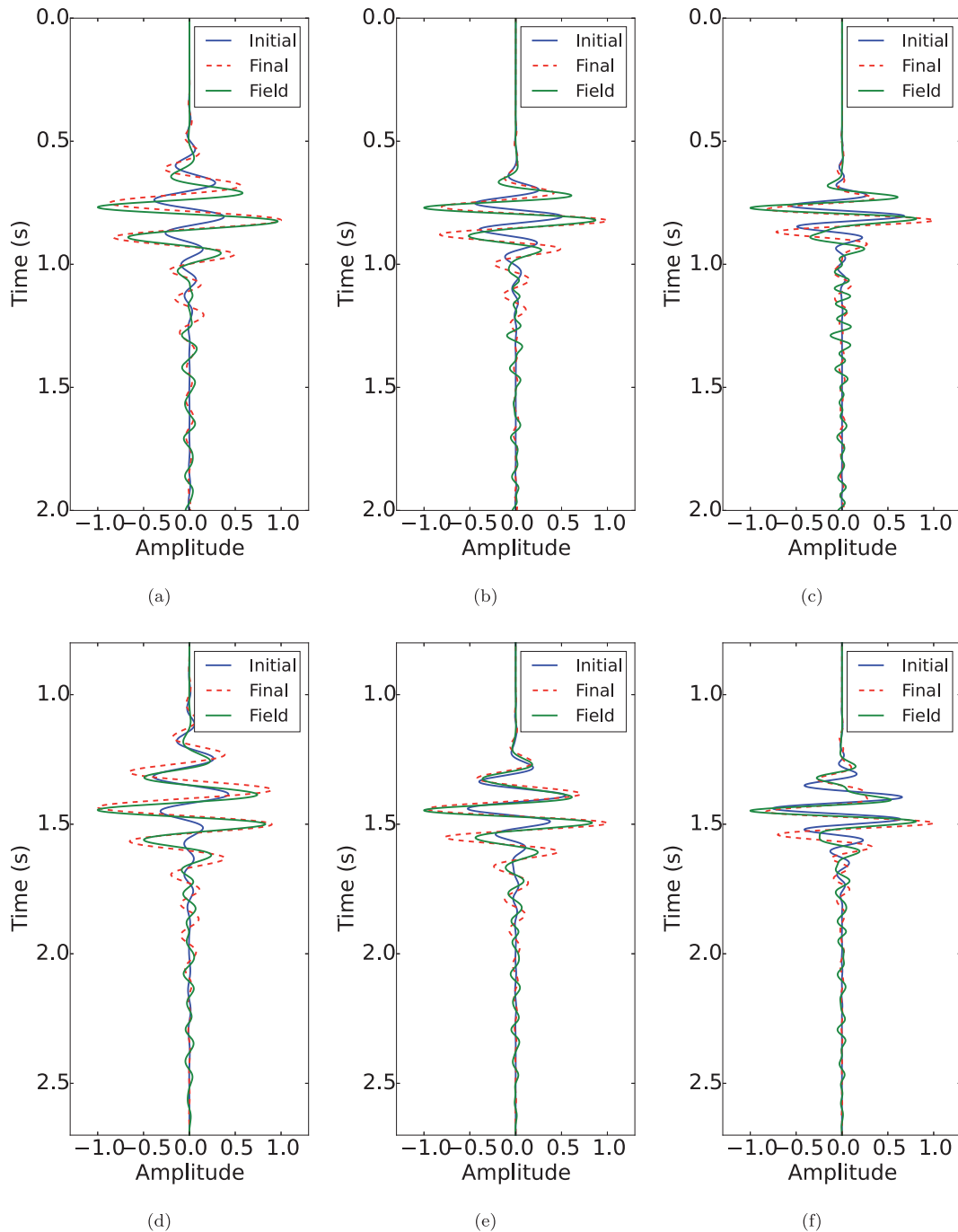
Figure 13. Trace comparisons of the synthetic data for the initial model, final model, and the field data in the three frequency bands. The top row is a trace from the center cable, whereas the bottom row is a trace from the outer cable. (a) and (d) 6–8 Hz, (b) and (e) 6–11 Hz, (c) and (f) 6–15 Hz.

continuity of the seismic events. From the common image point angle gathers comparison given in Fig. 18, we observe that for the final inverted model the gathers are flatter than for the initial model, which is an indication that the *P*-wave velocity model better explains the kinematics of the *P*-wave reflection events.

Fig. 19 shows a comparison of the smoothed well log from the exploration well (Fig. 3), and the initial and final inverted models. We observe that the inversion detects the events that are visible in the well log, but the magnitudes are wrong. At the largest depths, the updates are small in magnitude, as in the synthetic example. It is clear, however, that the final inverted model is closer to the well log than the initial model.

7 DISCUSSION

Elastic FWI is a computer intensive problem in 3-D due to the numerical methods used to compute the synthetic data and the model gradients. Although there has been an increase in computer power the last decade, we still need to restrict the number of grid cells in the models and use methods like the shot sub sampling method (Ha & Shin 2013), or the simultaneous-shot technique (Romero *et al.* 2000; Capdeville *et al.* 2005; Ben-Hadj-Ali *et al.* 2011), to be able to run the method within acceptable run times. It is promising that such methods can reduce the computational cost severely, and still produce reliable results as our examples demonstrate.
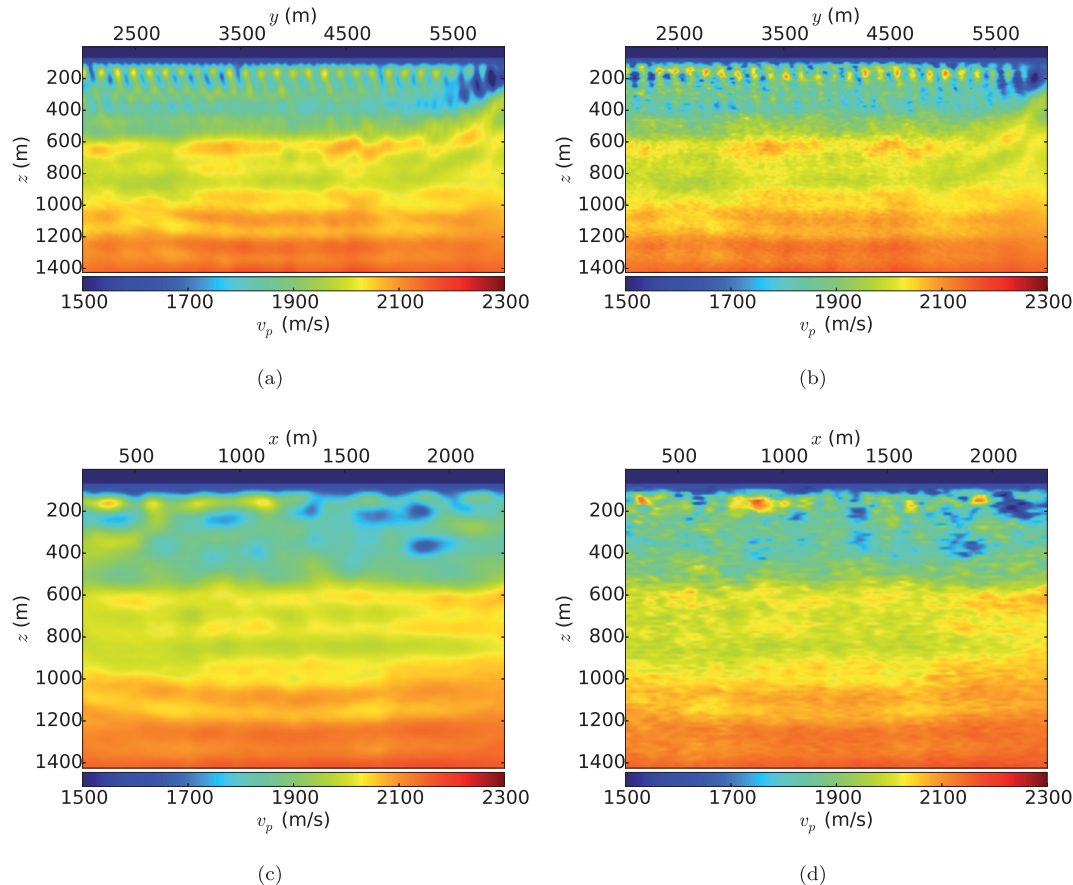
Figure 14. Vertical slices of the v_p model for the acoustic inversion of the field data set. The top row shows inline vertical slices at $x = 1162.5$ m, and the bottom row shows vertical slices at $y = 4000.0$ m. (a) and (c) inversion for v_p, updating ρ with empirical relationships, (b) and (d) inversion for v_p and ρ simultaneously.

The normalized misfit functional (eq. (5)) must be used with care when noise is present in the data. The consequence of the data normalization is that, if noise is present in the data, then the residuals and thus the gradient may be distorted. In the extreme case, a trace that contains only noise will become as important as a trace with little noise and clear data events. Since the gradients from each shot are stacked together to form the full gradient, any incoherent noise present in the data will contribute less than a coherent data event.

The preparation of the field data set to fit into the inversion work flow is a challenging task. The nearest neighbour technique for moving the receiver traces to a grid point is a possible error source for the inversion. However, with the numerical grid used in the inversion, a receiver is moved a small fraction of the wave lengths in the data at the receiver locations. The error could be reduced by using more accurate interpolation schemes (Choi & Munson 1998; Hindriks & Duijndam 2000; Özdemir *et al.* 2010). It is not clear that such techniques would work better due to the coarse and irregular trace sampling. Within all sources of error, the preprocessing steps performed before the field data set was released are of higher importance. Ideally, the data that is input to FWI should consist of raw unprocessed data. The preprocessing of the data using signal analysis methods can affect the ability of FWI to match the measured and simulated data, unless the simulated data is subject to the same preprocessing steps as the field data (see Section 3). The consequence of the restriction of the offset to 1700 m, as well as the reduction of the recording length to 2.3 s, is that wide-angle data are effectively removed from the data set. Furthermore, the swell-

noise and the low-cut frequency filters remove important signals from the data. The long-offset and the low frequency information are of fundamental importance for the successful resolution of the subsurface, in addition to preventing the inversion from running into a local minimum (Virieux & Operto 2009).

With the numerical grid and numerical differential operators used in the synthetic and field example, the modelling of the *S*-waves will be slightly affected by numerical dispersion. During the preliminary work with the field data set, this was considered to be problematic. Therefore, several tests were performed to investigate the impact of the numerical dispersion on the v_p update. The conclusion from these tests is that the update of v_p was not significantly affected by the small amount of numerical dispersion in the *S*-waves, since the wave modes are separated in the computation of the gradient (Dellinger & Etgen 1990). Therefore, the numerical grid was chosen such that some numerical dispersion is present in the *S*-waves to reduce the overall computational cost.

FWI is not independent of choice of parametrization (Tarantola 1986). The parameters of a given parametrization have a non-linear relation to the parameters of another parametrization (Mora 1987). An alternative to the (ρ, v_p, v_s) parametrization is (ρ, I_p, I_s) where I_p and I_s are the *P*-wave and *S*-wave impedances, respectively. The radiation pattern is different for the latter parametrization (Operto *et al.* 2013), which is favourable for short-offset data. However, it is not clear that the latter parametrization would work better due to the uncertainties in the data.
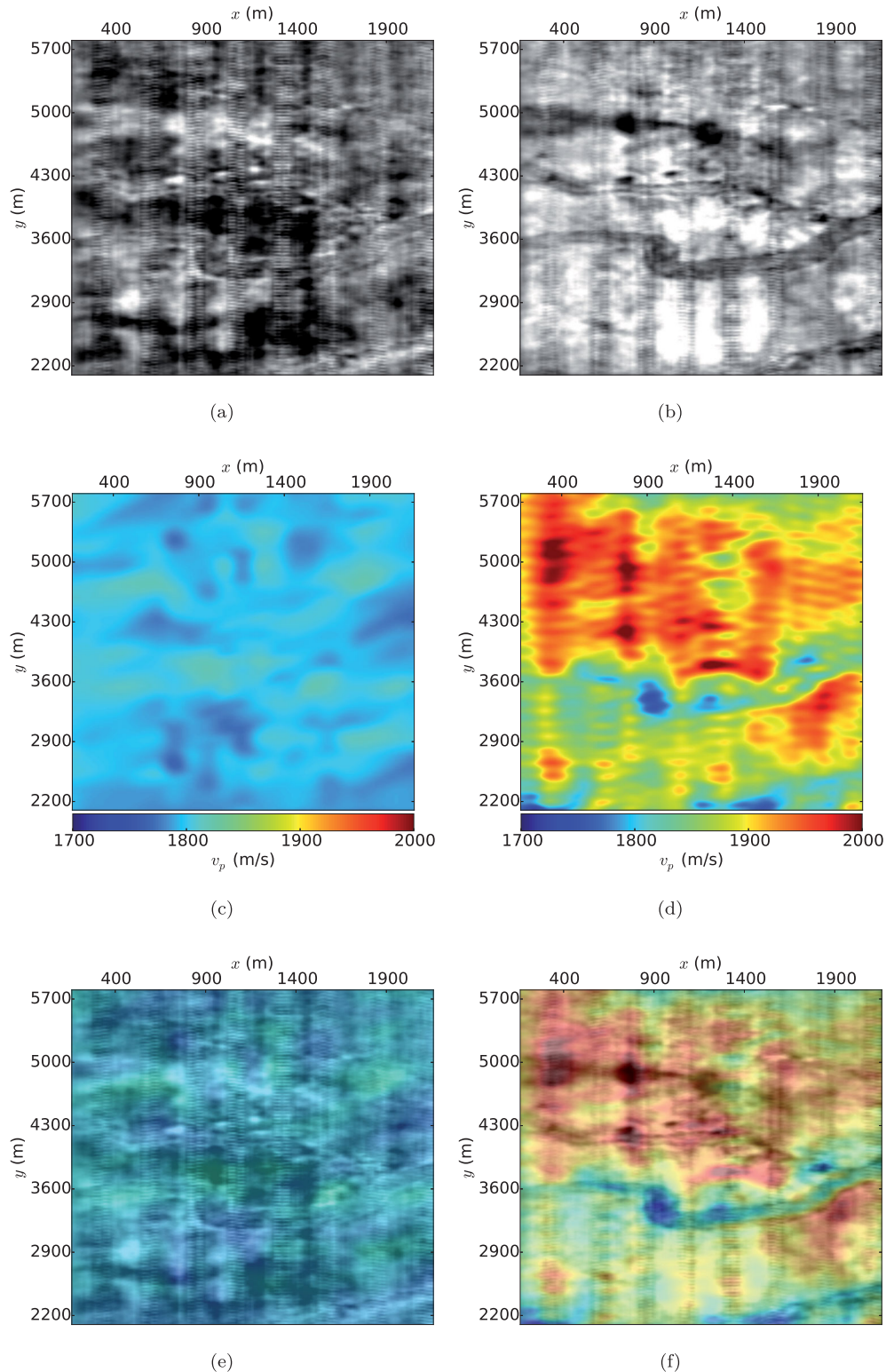
Figure 15. Horizontal slices at $z = 231.25$ m depth. (a) Seismic image with initial model, (b) seismic image with final model, (c) initial v_p model, (d) final v_p model, (e) overlay plot for the initial model, and (f) overlay plot for the final model. The coordinates on the plots are related to the coordinates in Fig. 4(a).

The inverted models from the synthetic and field data sets show that there are differences between acoustic and elastic inversion. For the field data set (Figs 11 and 14) the differences in magnitude for v_p are not as big as in the synthetic example (Figs 6 and 7). This can be explained by the magnitude of v_s, which for the field data set

is smaller than for the synthetic data set. This yields a low *S*-wave impedance contrast. When v_p and ρ are inverted for simultaneously using acoustic FWI, fine-grained artefacts appear in the model. The artefacts can be explained by the fact that ρ is difficult to invert for using FWI, particularly for short-offset data (Virieux & Operto
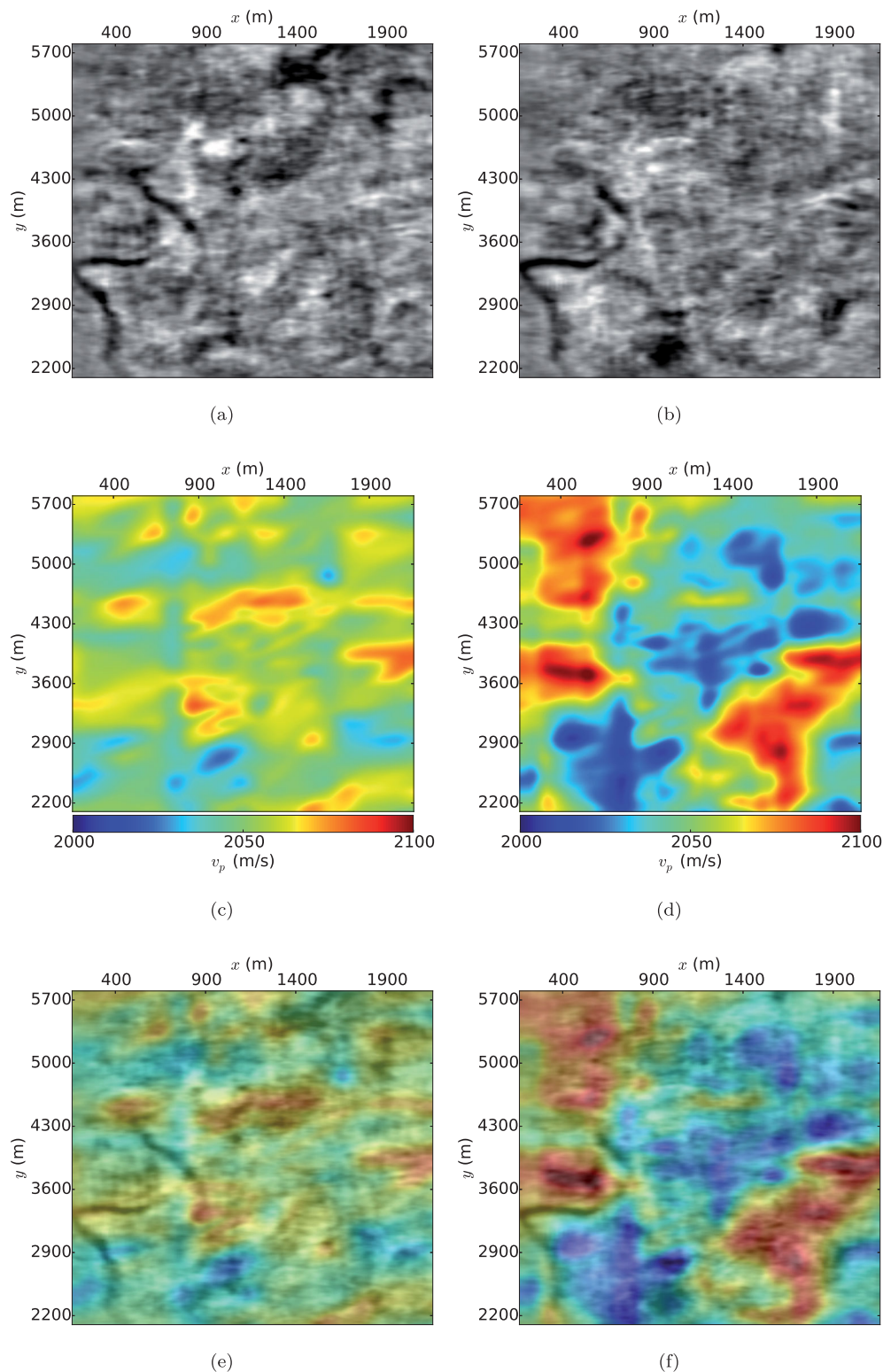
Figure 16. Horizontal slices at $z = 1043.75$ m depth. (a) Seismic image with initial model, (b) seismic image with final model, (c) initial v_p model, (d) final v_p model, (e) overlay plot for the initial model, and (f) overlay plot for the final model. The coordinates on the plots are related to the coordinates in Fig. 4(a).

2009), and that the solution space and thus the ill-posedness for the inverse problem increase when inverting simultaneously for ρ and v_p. Mulder & Plessix (2008) inverted successfully for v_p and ρ using acoustic FWI and elastic data, whereas Przebindowska *et al.* (2012) investigated the role of ρ in acoustic FWI and inverted

successfully for both v_p and ρ using acoustic data. Both studies used long-offset seismic data that are favourable for FWI (Virieux & Operto 2009). Thus, their results are not directly comparable with the results presented here. Barnes & Charara (2009) concluded that acoustic FWI could be used for short-offset data if there are
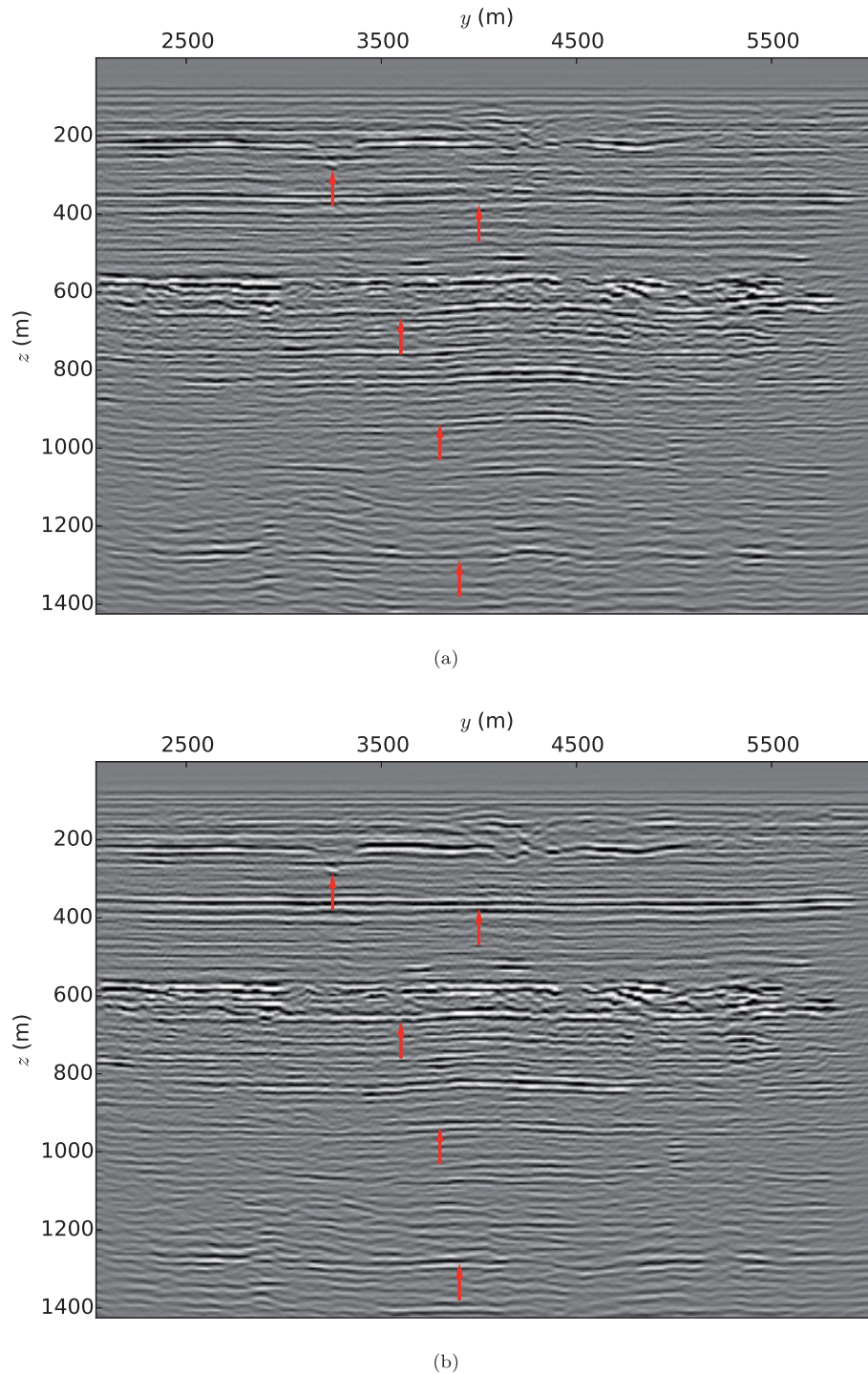
(a)

(b)

Figure 17. Seismic images at $x = 1162.5$ for using (a) the initial model and (b) the final inverted model. The arrows on the seismic images indicate positions where there are improvements in the image between the initial and final images.

low S-wave impedance constrasts and the initial model for v_p is accurately estimated. In our acoustic inversion, we experienced a shift downward in depth for the layers in the inverted acoustic models compared to the inverted elastic models. This, in addition to the artefacts in the sea bottom in the inverted acoustic models (Fig. 14), demonstrate that elastic FWI is important for producing reliable models for near-offset data.

One can question the validity of the two empirical relationships used (eqs 11 and 12) for the field data set. The density relationship is valid for many different rock types, whereas the S-wave relationship is valid for mud rocks (Gardner *et al.* 1974; Castagna *et al.* 1985). The choice of relationships was based on knowledge of the rock types in the specific area. We have tried to run the inversion using different empirical relationships, to investigate the sensitivity on the final inverted results. The conclusion is that, as long as the contrast between the water layer and the first sediments are not such that big amplitude surface waves are generated, the choice of S-wave relationship does not have major impact on the inversion results.
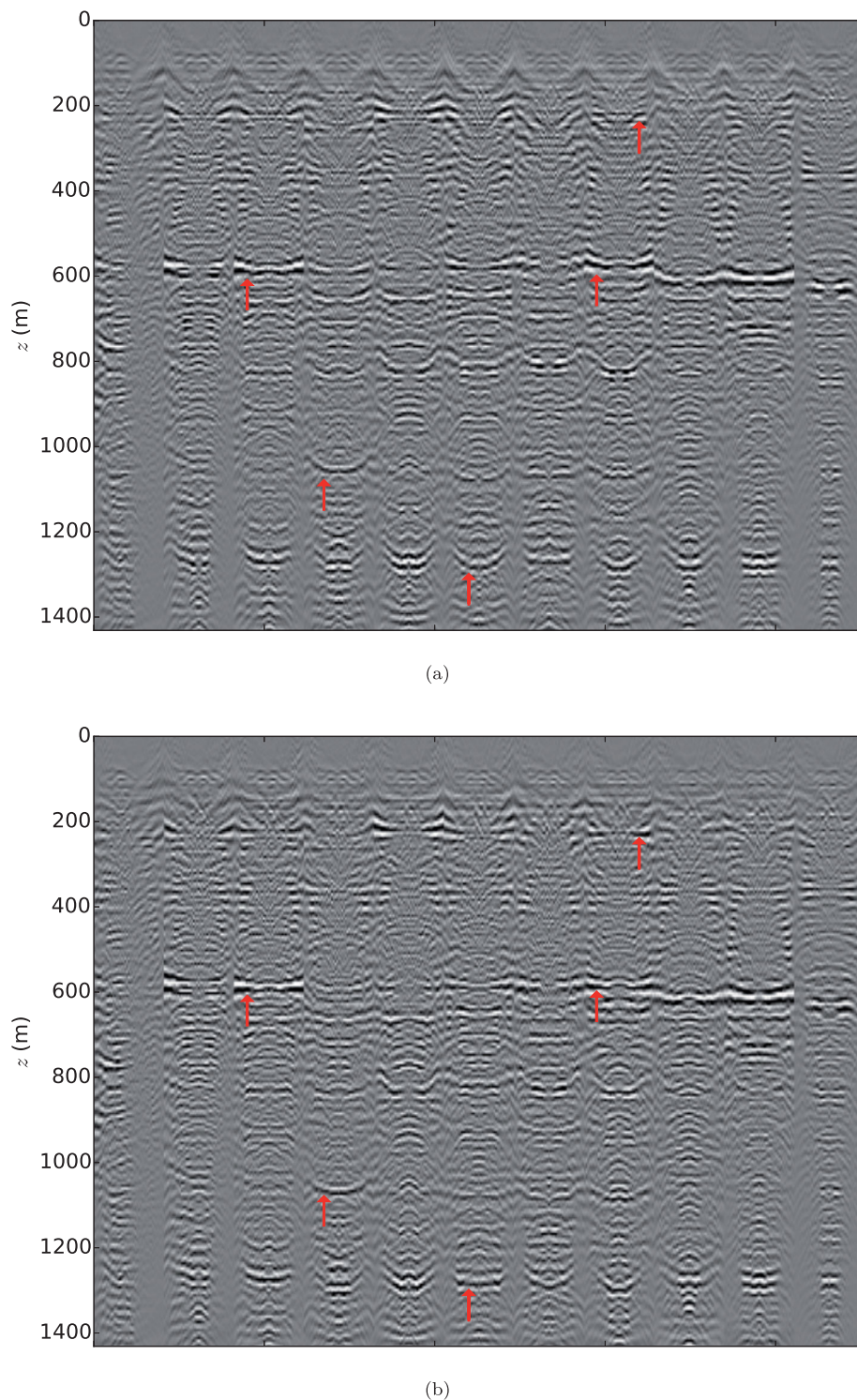
(a)

(b)

Figure 18. Common image point angle gathers: (a) initial model and (b) final model. The angle axis is between −50 and 50 degrees.

For the density, we tried to use a relationship estimated for the soft seabed sediments (Hamilton 1978), and the Gardner's relationship for the harder rock types. This procedure had minor effects on the inverted models. Hence, the inversion of the field data set is less sensitive to the choice of the density relationship.

It is clear from the above discussion that there are several uncertainties in the results for the field data set. This must be kept in mind when the results are interpreted. In the final seismic im-age (Fig. 17b), several clear and continuous interfaces are visible. The reflection interface at approximately 800 m depth is the top of the Utsira formation. The strong correlation between the inverted v_p model and the seismic images (Figs 15 and 16) demonstrate that FWI is capable of producing inverted models that explain the data better than, for instance, models produced using tomography. It is, however, not a perfect match, as can be seen in the compar-isons of the synthetic and real well log (Fig. 19). By comparing
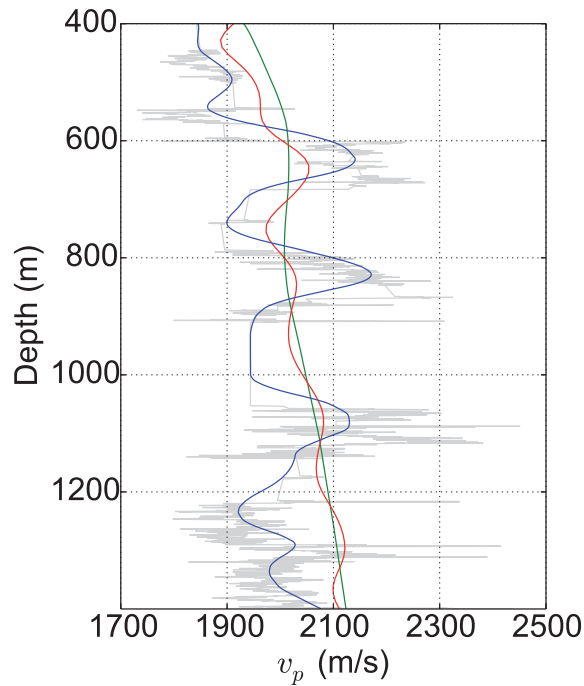
accounted for with a full 3-D approach than using the more limited 2-D methodology.

8 CONCLUSION

We have demonstrated an application of 3-D isotropic elastic FWI to a near-offset field data set consisting primarily of reflected waves. To investigate the assumptions and approximations in the inversion work flow, a synthetic sensitivity analysis was performed. The analysis demonstrated that for near-offset data, elastic FWI is superior to acoustic FWI due to wrong reflection and transmission coefficients in the latter method. The elastic FWI produces an elastic velocity model which reproduces the field data and can be used to produce conventional depth migrated images with improved resolution and continuity, and common image point angle gathers with improved flatness. This model also roughly matches the available well data.

Figure 19. Vertical profiles of the v_p model at the well position (grey line: sonic well log, blue line: smoothed sonic well log, green line: initial model, red line: inverted model).

the two well logs, we observe that several events are more or less correctly aligned in depth, but the amplitudes of the inverted events are wrong. If we compare the real well log with the vertical profiles from the synthetic example (Figs 5–9), we observe that the inversion has equal problems in the synthetic example, particularly at greater depths, where the events are visible, but with wrong magnitudes. The differences in magnitudes can be explained by the relatively short offsets and the frequency content used in the inversion (Sirgue & Pratt 2004; Virieux & Operto 2009). In addition, the well is placed on the edge of the data area (Fig. 4a), where the inversion results might be affected by edge effects. As a result, the resolution is not as good as it would have been if the well was placed in the middle of the area.

One of the benefits of elastic FWI is the possibility to estimate *S*-wave velocity models. We tried to invert for the *S*-wave velocity using the FWI framework. The inversion was only making minor updates in the upper part of the model, and ran quickly into a local minimum. This behaviour can be explained by the small amount of *S*-wave information in the field data set. Multi-component data might therefore be necessary to be able to invert successfully for *S*-waves (Sears *et al.* 2008, 2010; Raknes & Arntsen 2014b).

It is interesting to compare the results presented here with another study from the same area. Queißer & Singh (2013) performed 2-D elastic FWI using a single line from the Sleipner area. Compared to the work flow presented here, in their study they used 2-D modelling, a finer numerical grid and frequencies up to 80Hz. Their final inverted 2-D model (Queißer & Singh 2013, fig. 5) shows a clearly resolved layer at a depth of 600 m, and less clearly resolved layers at depths of 1000 m and 1100–1200 m. In general the velocity model is patchy and not well resolved below a depth of 800 m. In contrast the vertical slice of our full 3-D result (Fig. 11) is reasonably well resolved with layering for depths down to approximately 1200 m and correlates well with the well log for the major layers. This is to be expected since the physics of elastic wave propagation is better

REFERENCES

Abubakar, A., Pan, G., Li, M., Zhang, L., Habashy, T. & van den Berg, P., 2011. Three-dimensional seismic full-waveform inversion using the finite-difference contrast source inversion method, *Geophys. Prospect.,* **59**(5), 874–888.

Aki, K. & Richards, P.G., 2002. *Quantitative Seismology,* 2nd edn, University Science Books.

Auer, L., Nuber, A., Greenhalgh, S., Maurer, H. & Marelli, S., 2013. A critical appraisal of asymptotic 3D-to-2D data transformation in full-waveform seismic crosshole tomography, *Geophysics,* **78**(6), R235–R247.

Barnes, C. & Charara, M., 2009. The domain of applicability of acoustic full-waveform inversion for marine seismic data, *Geophysics,* **74**(6), WCC91–WCC103.

Ben-Hadj-Ali, H., Operto, S. & Virieux, J., 2008. Velocity model building by 3D frequency-domain, full-waveform inversion of wide-aperture seismic data, *Geophysics,* **73**(5), VE101–VE117.

Ben-Hadj-Ali, H., Operto, S. & Virieux, J., 2011. An efficient frequency-domain full waveform inversion method using simultaneous encoded sources, *Geophysics,* **76**(4), R109–R124.

Berenger, J.-P., 1994. A perfectly matched layer for the absorption of electromagnetic waves, *J. Comput. Phys.,* **114**, 185–200.

Brossier, R., Operto, S. & Virieux, J., 2009. Seismic imaging of complex onshore structures by 2D elastic frequency-domain full-waveform inversion, *Geophysics,* **74**(6), WCC105–WCC118.

Bunks, C., Saleck, F., Zaleski, S. & Chavent, G., 1995. Multiscale seismic waveform inversion, *Geophysics,* **60**(5), 1457–1473.

Butzer, S., Kurzmann, A. & Bohlen, T., 2013. 3D elastic full-waveform inversion of small-scale heterogeneities in transmission geometry, *Geophys. Prospect.,* **61**(6), 1238–1251.

Capdeville, Y., Gung, Y. & Romanowicz, B., 2005. Towards global earth tomography using the spectral element method: a technique based on source stacking, *Geophys. J. Int.,* **162**(2), 541–554.

Castagna, J., Batzle, M. & Eastwood, R., 1985. Relationships between compressional-wave and shear-wave velocities in clastic silicate rocks, *Geophysics,* **50**(4), 571–581.

Chadwick, R., Zweigel, P., Gregersen, U., Kirby, G., Holloway, S. & Johannessen, P., 2004. Geological reservoir characterization of a CO_2 storage site: the Utsira Sand, Sleipner, northern North Sea, *Energy,* **29**(9–10), 1371–1381.

Choi, H. & Munson, D.C., 1998. Analysis and design of minimax-optimal interpolators, *IEEE Trans. Signal Process.,* **46**(6), 1571–1579.

Choi, Y. & Alkhalifah, T., 2012. Application of multi-source waveform inversion to marine streamer data using the global correlation norm, *Geophys. Prospect.,* **60**, 748–758.

Dellinger, J. & Etgen, J., 1990. Wave-field separation in two-dimensional anisotropic media, *Geophysics,* **55**(7), 914–919.

Etgen, J., Gray, S. & Zhang, Y., 2009. An overview of depth imaging in exploration geophysics, *Geophysics,* **74**(6), WCA5–WCA17.

Fichtner, A., 2011. *Full Waveform Inversion Modelling and Inversion,* Springer-Verlag.

Fichtner, A., Bunge, H.-P. & Igel, H., 2006. The adjoint method in seismology: I—theory, *Phys. Earth planet. Inter.,* **157**, 86–104.

Fichtner, A., Kennett, B.L., Igel, H. & Bunge, H.-P., 2010. Full waveform tomography for radially anisotropic structure: new insights into present and past states of the australasian upper mantle, *Earth planet. Sci. Lett.,* **290**(3–4), 270–280.

Fichtner, A., Trampert, J., Cupillard, P., Saygin, E., Taymaz, T., Capdeville, Y. & Villaseñor, A., 2013. Multiscale full waveform inversion, *Geophys. J. Int.,* **194**(1), 534–556.

Furre, A.-K. & Eiken, O., 2014. Dual sensor streamer technology used in Sleipner CO_2 injection monitoring, *Geophys. Prospect.,* **62**(5), 1075–1088.

Gardner, G., Gardner, L. & Gregory, A., 1974. Formation velocity and density - the diagnostics basics for stratigraphic traps, *Geophysics,* **39**(6), 770–780.

Griewank, A. & Walther, A., 2000. Algorithm 799: revolve: an implementation of checkpointing for the reverse or adjoint mode of computational differentiation, *ACM Trans. Math. Soft.,* **26**(1), 19–45.

Ha, W. & Shin, C., 2013. Efficient laplace-domain full waveform inversion using a cyclic shot subsampling method, *Geophysics,* **78**(2), R37–R46.

Hamilton, E.L., 1978. Sound velocity-density relations in sea-floor sediments and rocks, *J. Acoust. Soc. Am.,* **63**, 366–377.

Hindriks, K. & Duijndam, A., 2000. Reconstruction of 3-D seismic signals irregularly sampled along two spatial coordinates, *Geophysics,* **65**(1), 253–263.

Holberg, O., 1987. Computational aspects of the choice of operator and sampling interval for numerical differentiation in large-scale simulation of wave phenomena, *Geophys. Prospect.,* **35**(6), 629–655.

Mavko, G., Mukerji, T. & Dvorking, J., 2009. *The Rock Physics Handbook,* 2nd edn, Cambridge Univ. Press.

Mittet, R., 2002. Free-surface boundary conditions for elastic staggered-grid modeling schemes, *Geophysics,* **67**(5), 1616–1623.

Mora, P., 1987. Nonlinear two-dimensional elastic inversion of multioffset seismic data, *Geophysics,* **52**(9), 1211–1228.

Mulder, W. & Plessix, R.-E., 2008. Exploring some issues in acoustic full waveform inversion, *Geophys. Prospect.,* **56**(6), 827–841.

Nocedal, J. & Wright, S.J., 2006. *Numerical Optimization,* 2nd edn, Springer Science+Business Media, LLC.

Operto, S., Gholami, Y., Prieux, V., Ribodetti, A., Brossier, R., Metivier, L. & Virieux, J., 2013. A guided tour of multiparameter full-waveform inversion with multicomponent data: from theory to practice, *Leading Edge,* **32**(9), 1040–1054.

Özdemir, K., Özbek, A., van Manen, D. & Vassallo, M., 2010. On data-independent multicomponent interpolators and the use of priors for optimal reconstruction and 3D up/down separation of pressure wavefields, *Geophysics,* **75**(6), WB39–WB51.

Plessix, R.-E., 2009. Three-dimensional frequency-domain full-waveform inversion with an iterative solver, *Geophysics,* **74**(6), WCC149–WCC157.

Pratt, R.G., 1999. Seismic waveform inversion in the frequency domain, part 1: theory and verification in a physical scale model, *Geophysics,* **64**(3), 888–901.

Przebindowska, A., Kurzmann, A., Köhn, D. & Bohlen, T., 2012. The role of density in acoustic full waveform inversion of marine reflection seismics, *74th EAGE Conference & Exhibition,* Copenhagen, Denmark.

Queißer, M. & Singh, S., 2013. Localizing CO_2 at Sleipner—seismic images versus p-wave velocities from waveform inversion, *Geophysics,* **78**(3), B131–B146.

Raknes, E. & Arntsen, B., 2014a. Time-lapse full-waveform inversion of limited-offset seismic data using a local migration regularization, *Geophysics,* **79**(3), WA117–WA128.

Raknes, E.B. & Arntsen, B., 2014b. Strategies for elastic full waveform inversion, in *SEG Technical Program Expanded Abstracts 2014,* pp. 1222–1226.

Ravaut, C., Operto, S., Improta, L., Virieux, J., Herrero, A. & Dell'Aversana, P., 2004. Multiscale imaging of complex structures from multifold wide-aperture seismic data by frequency-domain full-waveform tomography: application to a thrust belt, *Geophys. J. Int.,* **159**(3), 1032–1056.

Romero, L., Ghiglia, D., Ober, C. & Morton, S., 2000. Phase encoding of shot records in prestack migration, *Geophysics,* **65**(2), 426–436.

Sears, T., Singh, S. & Barton, P., 2008. Elastic full waveform inversion of multi-component obc seismic data, *Geophys. Prospect.,* **56**(6), 843–862.

Sears, T.J., Barton, P.J. & Singh, S.C., 2010. Elastic full waveform inversion of multicomponent ocean-bottom cable seismic data: application to alba field, u. k. north sea, *Geophysics,* **75**(6), R109–R119.

Shipp, R.M. & Singh, S.C., 2002. Two-dimensional full wavefield inversion of wide-aperture marine seismic streamer data, *Geophys. J. Int.,* **151**(2), 325–344.

Sirgue, L. & Pratt, R.G., 2004. Efficient waveform inversion and imaging: a strategy for selecting temporal frequencies, *Geophysics,* **69**(1), 231–248.

Sirgue, L., Etgen, J. & Albertin, U., 2008. 3D frequency domain waveform inversion using time domain finite difference methods, in *70th Annual International Conference and Exhibition,* EAGE.

Sirgue, L., Barkved, O., Gestel, J.V., Askim, O. & Kommedal, J., 2009. 3D waveform inversion on valhall wide-azimuth obc, in *71th Annual International Conference and Exhibition,* EAGE.

Symes, W.W., 2007. Reverse time migration with optimal checkpointing, *Geophysics,* **72**(5), SM213–SM221.

Tape, C., Liu, Q., Maggi, A. & Tromp, J., 2010. Seismic tomography of the southern california crust based on spectral-element and adjoint methods, *Geophys. J. Int.,* **180**(1), 433–462.

Tarantola, A., 1984. Inversion of seismic reflection data in the acoustic approximation, *Geophysics,* **49**(8), 1259–1266.

Tarantola, A., 1986. A strategy for nonlinear elastic inversion of seismic reflection data, *Geophysics,* **51**(10), 1893–1903.

Vigh, D. & Starr, E., 2008. 3D prestack plane-wave, full-waveform inversion, *Geophysics,* **73**(5), VE135–VE144.

Vigh, D., Jiao, K., Watts, D. & Sun, D., 2014. Elastic full-waveform inversion application using multicomponent measurements of seismic data collection, *Geophysics,* **79**(2), R63–R77.

Virieux, J., 1986. P-sv wave propagation in heterogeneous media: velocity-stress finite-difference method, *Geophysics,* **51**(4), 889–901.

Virieux, J. & Operto, S., 2009. An overview of full-waveform inversion in exploration geophysics, *Geophysics,* **74**(6), WCC1–WCC26.

Warner, M. *et al.*, 2013. Anisotropic 3D full-waveform inversion, *Geophysics,* **78**(2), R59–R80.

Zhen, Q., Minghui, L., Xiaodong, Z., Yao, Y., Cai, Z. & Jianyong, S., 2009. The implementation of an improved NPML absorbing boundary condition in elastic wave modeling, *Appl. Geophys.,* **6**(2), 113–121.